Noise Suppression of Corona Current Measurement From HVdc Transmission Lines

Qiusheng Wang, Deepa Kundur, *Fellow, IEEE*, Haiwen Yuan, Yuanqing Liu, Jiayu Lu, and Zhao Ma

***Abstract*— The complexity and diversity of noise in corona current measurements of high-voltage direct current (HVdc) transmission lines leads to challenges in estimating corona performance. This paper proposes an offline noise suppression method for HVdc corona current measurements. Given that the corona current and background noise processes coexist within the same frequency band, we develop a novel multifaceted filtering approach for HVdc corona currents. Specifically, a cross correlation function-based center frequency recognition method is presented to provide filter design specification for a multiple notch filter to suppress narrow-band radio interference. To then suppress the residual full-band noise, wavelet denoising techniques with hard and soft thresholds are applied and compared. The proposed noise suppression method is applied to field-measured corona current data from the HVdc Experimental Base in China. We assert that the noise suppression method has versatile implementation and can be readily applied for corona loss estimation of HVdc systems.**

***Index Terms*— Corona current, corona performance, cross correlation function, high-voltage direct current (HVdc), multiple notch filter, noise suppression, particle swarm optimization (PSO), wavelet transform.**

I. Introduction

HIGH-VOLTAGE direct-current (HVdc) transmission systems have advantages including bulk-power and long-distance transmission, high reliability, and low cost [1]–[3]. The high voltages cause strong electric fields near the surface of the conductors of transmission lines. Self-sustaining ionizing partial discharges (coronas) occur when the electric field intensity exceeds a critical value [4], [5]. Corona performance is defined in terms of corona loss (CL), radio interference (RI), audible noise, ground-level electric field, and ion current density. It must be evaluated and controlled for HVdc transmission system design and construction [6]–[8].

Manuscript received January 13, 2015; revised July 20, 2015; accepted July 27, 2015. Date of publication November 10, 2015; date of current version January 4, 2016. This work was supported in part by the National Natural Science Foundation of China under Grant NSFC-61273165, in part by the National Natural Science Foundation of China under Grant NSFC-51207005, and in part by the Thousand Talents Program through the State Grid Corporation of China under Grand EPRIPDKJ (2014) 2863. The Associate Editor coordinating the review process was Dr. Edoardo Fiorucci.

Q. Wang and H. Yuan are with the School of Automation Science and Electrical Engineering, Beihang University, Beijing 100191, China (e-mail: wangqiusheng@buaa.edu.cn; yhw@buaa.edu.cn).

D. Kundur is with the Edward S. Rogers Sr. Department of Electrical and Computer Engineering, University of Toronto, Toronto, ON M5S 3G4, Canada (e-mail: dkundur@ece.utoronto.ca).

Y. Liu, J. Lu, and Z. Ma are with the China Electric Power Research Institute, Beijing 100192, China (e-mail: liuyq@epri.sgcc.com.cn; lujy@epri.sgcc.com.cn; mazhao@epri.sgcc.com.cn).

Color versions of one or more of the figures in this paper are available online at http://ieeexplore.ieee.org.

Digital Object Identifier 10.1109/TIM.2015.2485339

The corona discharge studies of HVdc transmission lines are typically approached numerically or experimentally [9]–[11]. Several efficient and effective numerical approaches have been developed in [9] and [10]. Experimental methods, in contrast, are expensive and somewhat arduous to conduct, but can lead to a direct and actual indication and characterization of corona discharge from corona current measurements [1], [9], [12].

The actual corona current represents a weak wideband signal measured under conditions of high-voltage stress [12]. Because HVdc transmission lines are exposed to the natural elements, it is affected by various factors, including geometry of the associated conductor, power supply quality, electric field intensity, conductor surface smoothness, temperature, moisture, wind speed, air pressure, RI, and decaying organic matter such as animal excretions. Moreover, many of these aspects are coupled thus resulting in an overall complex influence on measured corona current [12]–[15].

To analyze CLs and characterize secondary effects accurately, the existing noise in corona current must first be sufficiently reduced. This poses several challenges due to [12]–[17]: 1) the lack of accurate mathematical models to represent the actual corona current; 2) the wideband nature of corona current ranging from few hertz to tens of megahertz; 3) the existence of specialized noise such as narrow-band radio disturbance; and 4) the limitations of denoising methods in adapting to a variety of noise sources.

As one of the key steps of CL estimation, filtering of HVdc corona current noise represents an open problem that we consider in this paper. Although a large number of denoising methods have been developed for a variety of applications including speech and image processing [18], the unique characteristics of corona current and its measurement makes direct application of the existing techniques inappropriate. We assert that effective denoising should account for the properties of the corona measurement system, which this paper addresses.

In a related work, Otto and Reader [19] investigate the wideband and narrow-band HVdc conductor corona test methods for radio noise prediction. Sriram *et al.* [16] propose a denoising method for partial discharge signals; several techniques are investigated and employed on simulated and real partial discharge data. Similarly, Evagorou *et al.* [17] employ a wavelet packet-based transform to extract the partial discharge signals from noise. Although these contributions are loosely related to our problem of noise reduction in HVdc corona current, they provide useful reference for the development of our noise suppression method.

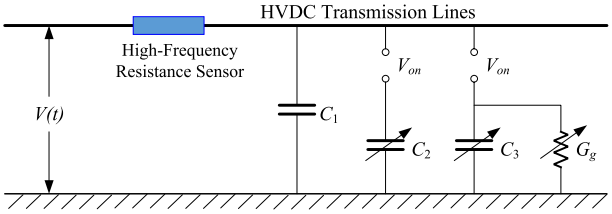

Fig. 1. Equivalent circuit model for HVdc corona current [2].

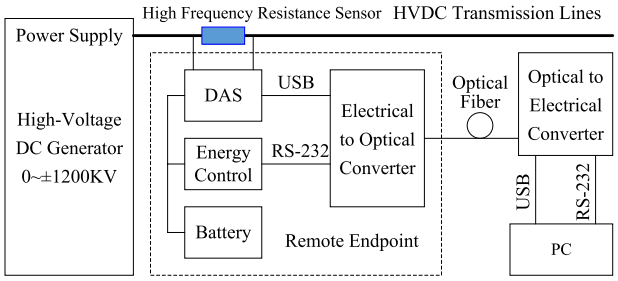

Fig. 2. Schematic of HVdc corona current measurement system.

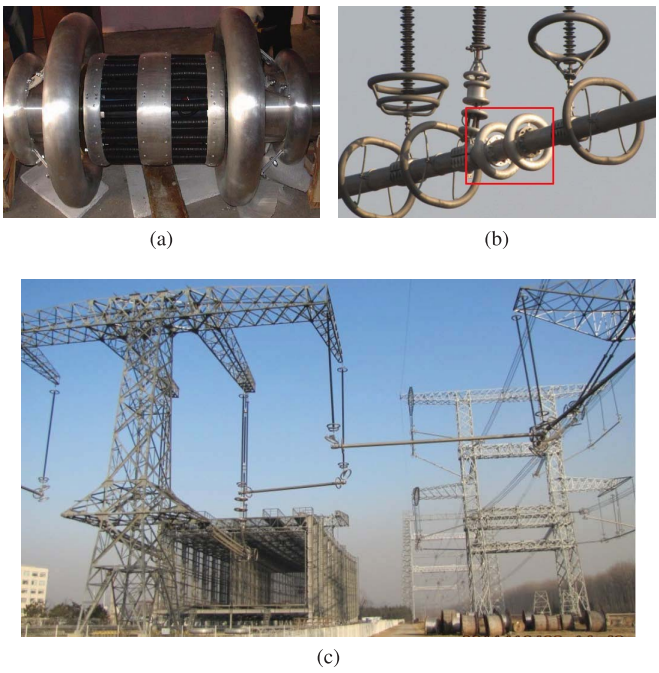

Fig. 3. High-frequency resistance sensor and corona current and background noise measurement platform. (a) High-frequency resistance sensor. (b) High-frequency sensor on test line. (c) Corona current measurement platform.

This paper is organized as follows. The proposed denoising scheme for noise suppression of HVdc corona current is highlighted in Section II. Mathematical models and a cross correlation function-based analysis method are presented in Section III. Section IV proposes an optimal design technique for multiple notch filters to attenuate narrow-band RI. Then, Section V presents a wavelet denoising approach to suppress full-band noise. The performance of the proposed noise suppression method is evaluated using the field-measured corona current data in Section VI with the conclusions in Section VII.

II. Proposed Noise Suppression Scheme

A. Corona Current Measurement System

It has recently been shown that the HVdc corona current can be physically represented by the nonlinear RC circuit shown in Fig. 1. Here, C_1 is the geometric capacitance related to the conductor configuration, C_2 is the nonlinear capacitance due to the corona itself, C_3 is the additional capacitance related to the charge loss to the air, G_g represents the nonlinear conductance due to CL, $V(t)$ is the transmission line voltage, and $V_{\rm ON}$ is the corona onset voltage (the critical voltage of the occurrence of corona discharge). A high-frequency resistance sensor is installed in series on the HVdc transmission line conductor.

If $V(t) < V_{\rm ON}$, then $C_2 = C_3 = G_g = 0$, and there only exists wire-to-ground charging current and a small amount of leakage current from insulators. In particular, if $V(t) = 0$, there are no charging and leakage currents and the *background noise* is only captured by the high-frequency resistance sensor. If $V(t) > V_{\rm ON}$, G_g surges rapidly, while C_2 and C_3 rise slowly with the increase of $V(t)$. Consequently, the *corona current* (the current through the resistance sensor minus the negligible leakage current of insulators) is measured by the high-frequency resistance sensor.

To measure the corona current, a high-frequency sensor-based measurement system scheme is proposed for HVdc transmission lines, as shown in Fig. 2. The corona current measurement system is controlled and managed by a ground-based PC workstation. Under different voltage conditions, $V(t) > V_{\rm ON}$ or $V(t) = 0$, the sensor measures the corona current or background noise, respectively, which is then transmitted to a central database through high-speed optical fibers. Thus, the database contains both the readings of noisy corona current and background noise obtained during different time intervals by the same sensor.

Fig. 2 was realized at the HVdc Experimental Base of the China Electrical Power Research Institute, Beijing, China. The development of the high-frequency resistance sensor and corona current measurement system were discussed in [2]. The actual sensor (with small grading rings to avoid corona discharges at both ends) is implemented by parallel noninductive resistors whose maximum operating frequencies are higher than 5 MHz. It has been installed in series on the HVdc experimental lines, shown in Fig. 3. The system provides the actual corona current and background noise employed in this paper to verify the proposed offline noise suppression method of corona current.

B. Noise Suppression

HVdc transmission lines exposed to the natural elements are well known to act as large antennas thus receiving various forms of interference including components from civilian radio broadcasts that are narrowband in nature. At the same time, wideband noise (such as thermal noise) is recorded by the corona current measurement system of Section II-A. With reference to the measurement output, it is clear that when $V(t) = 0$, the measurement consists solely of background noise comprised of RI and full-band noise. When $V(t) > V_{\rm ON}$, the measurement system detects the corona current including RI and full-band noise.

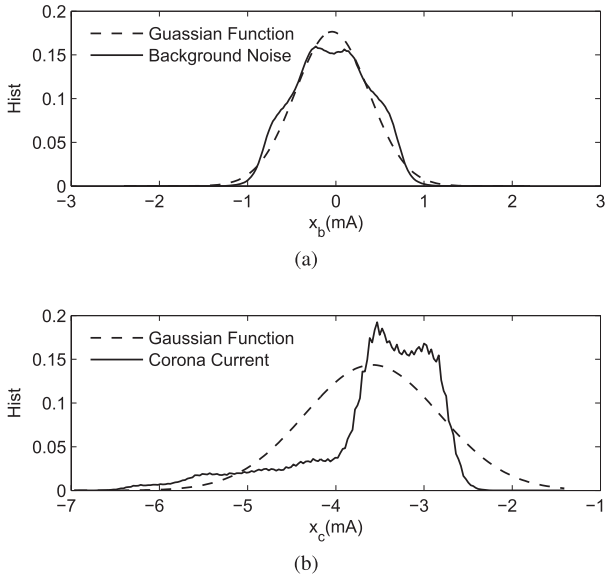

Fig. 4. Normalized histograms of measured (a) background noise and (b) corona current (−800 kV). The Gaussian functions are evaluated by the estimated mean and variance values of the measurements in (a) or (b).

The HVdc corona currents are affected by a variety of factors including the presence of significant and time-varying radio broadcast communications. Thus, one cannot invoke the central limit theory to approximate the noise as Gaussian. We show the normalized histograms of the HVdc measurements in Fig. 4. It is clear that the measurements are non-Gaussian in nature. This deviation makes the estimation of corona performance such as CL difficult to compute accurately. Moreover, the diverse characteristics of the RI component (narrowband) and other components such as thermal noise (wideband) require a multifaceted filtering method. Hence, we propose an *informed* filtering approach that makes use of the recorded corona-free background measurement readings to improve the noise reduction process.

To facilitate the discussion, the term *narrow-band RI* refers solely to the components from amplitude modulation (AM) broadcasts or other radio communications. Particularly, the center carrier frequency and bandwidth of each interfering AM broadcast are assumed to be fixed. Moreover, the magnitude of the carrier component is considered to be far higher than those of sidebands. This particular spectral structure facilitates notch filter design for narrow-band interference removal.

We exploit the somewhat static characteristics of narrow-band RI, during both the presence and absence of corona, to identify its associated carrier frequencies using a cross correlation function-based approach. Once the narrow-band interference regions are determined, a high-performance multiple notch filter is employed to preserve most of the corona signal. For the remaining *wideband residual noise*, which does not exhibit a well-defined frequency separation from the corona, multiresolution wavelet denoising is applied.

Our offline noise suppression approach is presented in Fig. 5. First, we make use of two distinct measurements from the high-frequency resistance sensor representing the noisy corona current and sole background noise that are measured at distinct times when $V(t) > V_{\mathrm{ON}}$ and $V(t) = 0$, respectively. Second, the narrow-band RI components are enhanced by cross correlating the two measurements. Third, the multiple notch filter is optimally designed to remove the narrow-band interference. Finally, the wavelet denoising technique is applied. Thus, in our framework, we also assume that the time interval between the two measurements (with and without corona) is short enough (e.g., within 48 h) to facilitate the carrier frequency identification, and the voltages of HVdc transmission lines are stable such that the corona current can be regarded as a constant value in statistical sense.

III. Narrow-Band Radio Component Identification

A. Models and Representation

As discussed in the previous section, when $V(t) = 0$ in Fig. 1, the high-frequency resistance sensor measures the background noise $b(t)$ comprised of two terms

$$b(t) = d(t) + o(t) \tag{1}$$

where $d(t)$ is the narrow-band RI primarily from AM broadcasts and $o(t)$ represents the residual wideband noise. Thus, in the frequency domain, we have

$$B(\Omega) = D(\Omega) + O(\Omega) \tag{2}$$

where $B(\Omega)$, $D(\Omega)$, and $O(\Omega)$ are the Fourier transforms of $b(t)$, $d(t)$, and $o(t)$, respectively.

To facilitate the analysis, we assign all carrier components of the narrow-band RI to $d(t)$ while including the corresponding sideband components in $o(t)$. Suppose $d(t)$ contains M carrier components. Hence, we can model its spectrum as the following superposition:

$$D(\Omega) = \sum_{i=1}^{M} D_i \delta(\Omega - \Omega_i) \tag{3}$$

where D_i and Ω_i are the magnitude and frequency related with ith carrier term.

Similarly, for $V(t) > V_{\mathrm{ON}}$ in Fig. 1, the measurement reading $x(t)$ consists of the superposition of three terms

$$x(t) = s(t) + r(t) + n(t) \tag{4}$$

where $s(t)$ is the noiseless corona current, and $r(t)$ and $n(t)$ are analogous to $d(t)$ and $o(t)$ defined in (1), respectively. Note that, we assume that the low-frequency harmonic noise from rectification (i.e., imperfect high voltage alternating current (HVAC) to HVdc conversion) is removed in advance given that it is known to be in the frequency band less than 2 kHz.

In the frequency domain, we have

$$X(\Omega) = S(\Omega) + R(\Omega) + N(\Omega) \tag{5}$$

where $X(\Omega)$, $S(\Omega)$, $R(\Omega)$, and $N(\Omega)$ are the Fourier transforms of $x(t)$, $s(t)$, $r(t)$, and $n(t)$, respectively. According to our assumption in Section II-B, the noiseless corona current is a constant value in statistical sense, i.e., $s(t) = C, \forall\ t$; hence, the spectrum of $s(t)$ is

$$S(\Omega) = 2\pi C \delta(\Omega). \tag{6}$$

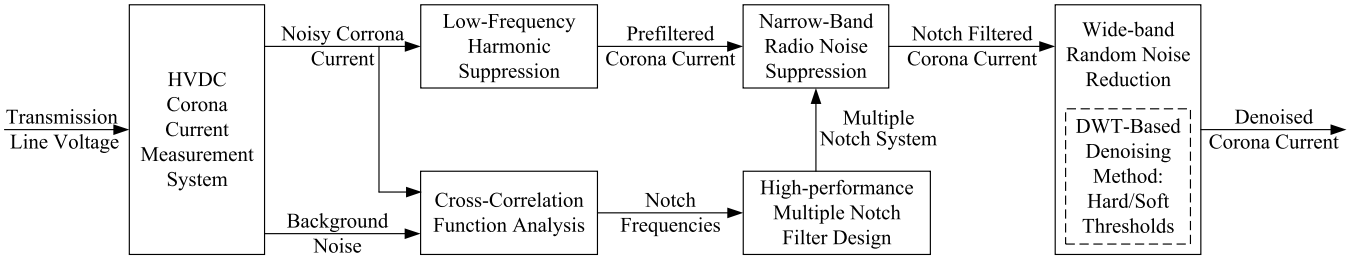

Fig. 5. Proposed HVdc corona current noise suppression approach. The noisy corona current and background noise readings from the measurement system are obtained from the same high-frequency sensor, but at distinct times.

TABLE I
TERMS OF $\Phi_{xb}(j\Omega)$

	$s(t)$	$r(t)$	$n(t)$
$d(t)$	$\Phi_{sd}(\Omega)$	$\Phi_{rd}(\Omega)$	$\Phi_{nd}(\Omega)$
$o(t)$	$\Phi_{so}(\Omega)$	$\Phi_{ro}(\Omega)$	$\Phi_{no}(\Omega)$

Analogous to $d(t)$, the spectrum of $r(t)$ is modeled as

$$R(\Omega) = \sum_{i=1}^{M} R_i \delta(\Omega - \Omega_i) \tag{7}$$

where R_i and Ω_i are the magnitude and frequency related with ith carrier term. Particularly, Ω_i in (3) is the same as Ω_i in (7) due to the coupled AM broadcasts having the same carrier frequencies in $d(t)$ and $r(t)$.

Given the presence of strong frequency components at Ω_i in both $D(\Omega)$ and $R(\Omega)$ as well as the wideband nature of $O(\Omega)$ and $N(\Omega)$, we apply a cross correlation function operator to $b(t)$ and $x(t)$ to enhance their jointly invariant characteristics hence identifying the values of Ω_i, for $i = 1, 2, \ldots, M$.

B. Narrow-Band Interference Component Recognition

The cross correlation function of two deterministic signals $f(t)$ and $g(t)$ is defined as

$$\phi_{fg}(\tau) = \int_{-\infty}^{\infty} f(t+\tau) g^*(t) d\tau. \tag{8}$$

Given that $F(\Omega)$ and $G(\Omega)$ are the Fourier transforms of $f(t)$ and $g(t)$, respectively, the Fourier transform of $\phi_{fg}(t)$ can be expressed as [20], [21]

$$\Phi_{fg}(\Omega) = \frac{1}{2\pi} F(\Omega) G^*(\Omega). \tag{9}$$

Since our aim is to identify the values of $\Omega_i, \forall\, i$, we take a frequency-domain perspective, which is also computationally more feasible. To compute $\Phi_{xb}(\Omega)$, the cross correlation function of the measured noisy corona current $x(t)$ and the corona-free background noise $b(t)$, we make use of its additive structure

$$\begin{aligned}\Phi_{xb}(\Omega) = {} & \Phi_{sd}(\Omega) + \Phi_{so}(\Omega) + \Phi_{rd}(\Omega) + \Phi_{ro}(\Omega) \\ & + \Phi_{nd}(\Omega) + \Phi_{no}(\Omega).\end{aligned} \tag{10}$$

Table I summarizes the individual additive terms that comprise $\Phi_{xb}(j\Omega)$, which we analyze as follows.

1) Cross Correlation Function of s(t) and d(t):

$$\Phi_{sd}(\Omega) = \frac{1}{2\pi} S(\Omega) D^*(\Omega) = 0 \tag{11}$$

since $\Omega_i \neq 0, \forall\, i$ which implies that the Dirac delta functions of $S(\Omega)$ and $D^*(\Omega)$ do not overlap. This implies that the corona current is uncorrelated from the narrow-band RI, which is reasonable as both components would be expected, physically, to be independent.

2) Cross Correlation Function of s(t) and o(t): Using the sifting property

$$\Phi_{so}(\Omega) = \frac{1}{2\pi} S(\Omega) O^*(\Omega) = \frac{1}{2\pi} O^*(0) \delta(\Omega) = \frac{1}{2\pi} O(0) \delta(\Omega) \tag{12}$$

where $O(0) = \int_{-\infty}^{\infty} o(t) dt \in \mathbb{R}$, which implies $O^*(0) = O(0)$. Thus, the contribution of $\Phi_{so}(\Omega)$ will be at dc, which may be removed or neglected when identifying $\Omega_i, \forall\, i$.

3) Cross Correlation Function of r(t) and d(t): From sifting

$$\Phi_{rd}(\Omega) = \frac{1}{2\pi} R(\Omega) D^*(\Omega) = \sum_{i=1}^{M} \bar{K}_i \delta(\Omega - \Omega_i) \tag{13}$$

where $\bar{K}_i = R_i D_i / (2\pi)$, for $i = 1, 2, \ldots, M$, which illustrates how the AM carrier signals are enhanced by the cross correlation function operation that will result in large peaks for $\Omega = \Omega_i, \forall\, i$.

4) Cross Correlation Function of r(t) and o(t): Similarly

$$\Phi_{ro}(\Omega) = \frac{1}{2\pi} R(\Omega) O^*(\Omega) = \sum_{i=1}^{M} \hat{K}_i \delta(\Omega - \Omega_i) \tag{14}$$

where $\hat{K}_i = R_i \cdot O^*(\Omega_i)/(2\pi)$, for $i = 1, 2, \ldots, M$. Thus, $\Phi_{ro}(\Omega)$ also enhances the components at $\Omega = \Omega_i, \forall\, i$.

5) Cross Correlation Function of n(t) and d(t):

$$\Phi_{nd}(\Omega) = \frac{1}{2\pi} N(\Omega) D^*(\Omega) = \sum_{i=1}^{M} \check{K}_i \delta(\Omega - \Omega_i) \tag{15}$$

where $\check{K}_i = D_i \cdot N(\Omega_i)/(2\pi)$, for $i = 1, 2, \ldots, M$ further enhancing the components at $\Omega = \Omega_i, \forall\, i$.

6) Cross Correlation Function of n(t) and o(t): We consider the final component

$$\Phi_{no}(\Omega) = \frac{1}{2\pi} N(\Omega) O^*(\Omega) \tag{16}$$

to be full band in nature, since $N(\Omega)$ and $O(\Omega)$ are both in general wideband.

The components $\Phi_{sd}(\Omega)$ and $\Phi_{so}(\Omega)$ are negligible; the latter because the spike at $\Omega = 0$ can be removed or ignored. Moreover, $\Phi_{rd}(t)$, $\Phi_{ro}(t)$ and $\Phi_{nd}(t)$ can be combined due to their common structure as follows:

$$\Phi_{rc}(\Omega) = \Phi_{rd}(\Omega) + \Phi_{ro}(\Omega) + \Phi_{nd}(\Omega) = \sum_{i=1}^{M} K_i \delta(\Omega - \Omega_i) \tag{17}$$

where $K_i = \bar{K}_i + \hat{K}_i + \check{K}_i$, for $i = 1, 2, \ldots, M$. Hence, (10) can be simplified to

$$\Phi_{xb}(\Omega) = \Phi_{rc}(\Omega) + \Phi_{no}(\Omega). \tag{18}$$

The former term has M distinguishing spectral peaks at $\Omega = \Omega_i$, while the later has a wideband characteristic that is weaker within its frequency range. Thus, the cross correlation function allows the recognition of $\Phi_{rc}(\Omega)$ and hence the estimation of Ω_i $(i = 1, 2, \ldots, M)$ from $\Phi_{xb}(\Omega)$. The practical feasibility of this approach is studied in Section VI.

The cross correlation function of background noise and corona current establishes a theoretical foundation for narrow-band radio component recognition. Once the carrier frequencies of the narrow-band RI components have been identified, a high-performance multiple notch filter is designed for its removal.

IV. Narrow-Band Radio Interference Suppression

Because the corona current and background noise are recorded in digital format, typically via a sample-and-hold and amplitude quantization, the analog representations of Section III are converted to digital ones; specifically, analog frequency is converted to normalized digital frequency via the relation $\omega = \Omega / F_s$, where F_s is the sampling frequency. Hence, $\omega_i = \Omega_i / F_s$ for $i = 1, 2, \ldots, M$.

A. Design Specifications of Multiple Notch Filter

The frequency response of an ideal digital filter with M notch frequencies is defined as [22]

$$H_d(e^{j\omega}) = \begin{cases} 0, & \omega = \omega_i \\ 1, & \omega \neq \omega_i \end{cases} \tag{19}$$

where ω_i is the ith notch frequency, for $i = 1, 2, \ldots, M$. The reader should note that the frequency response of a realizable notch filter is an approximation of $H_d(e^{j\omega})$ whose specifications are determined by the notch frequencies and associated bandwidths shown, for instance, in Fig. 6, where $H(e^{j\omega})$ satisfies $|H(e^{j\omega_i})| = 0$ and $|H(e^{j(\omega_i \pm \Delta\omega_i/2)})| = \sqrt{2}/2$, for $i = 1, 2, \ldots, M$.

There are three well-known methods to approximate $H_d(e^{j\omega})$. The cascading method [23] is the simplest, but the results in uncontrollable gains between notch frequencies. The two-stage optimal approach [24] can be used to design a stable multiple notch filter, but requires the solution of a complex quadratic programming problem. Finally, the all-pass filter-based method [22] can obtain an accurate magnitude response, but at the cost of possible illconditioning of intermediate linear equations constructed in design process.

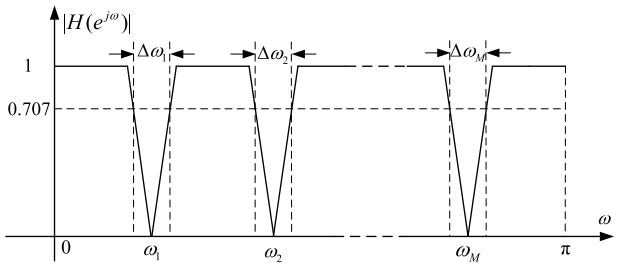

Fig. 6. Multiple notch filter design specifications.

Algorithm 1 Original PSO [29]

1: Initialize a population array of K particles with random positions and velocities denoted by arrays X and V, respectively, in an M-dimensional search space.
2: **loop**
3: For the k-th particle (for $k = 1, 2, \ldots, K$), evaluate the desired *optimization fitness function* at the M-dimensional position X_k.
4: Compare each particle's fitness evaluation with its historically best value denoted P_{best}. If current value is better than P_{best}, then set P_{best} equal to the current fitness evaluation value, and set P_k to equal the current location X_k in the M-dimensional space.
5: Identify the particle in the neighborhood with the best *success* (fitness value) so far, and assign its index to the variable g thus denoting its position P_g.
6: Change the velocity V_k and position X_k of the k-th particle according to the following equation:

$$\begin{cases} V_k \leftarrow V_k + U(0, \phi_1) \otimes (P_k - X_k) \\ \qquad\quad + U(0, \phi_2) \otimes (P_g - X_k) \\ X_k \leftarrow X_k + V_k \end{cases} \tag{20}$$

where $U(0, \phi_i)$ is a random vector with uniform distribution in $[0, \phi_i]$, V_k is kept within $[-V_{k\max}, +V_{k\max}]$ and $\otimes$ is component-wise multiplication.
7: If a criterion is met (usually a sufficiently good fitness or a maximum number of iterations), exit loop.
8: **end loop**

To overcome the shortcomings of the classical multiple notch filter design methods, we propose a novel design approach in the following section using the carrier frequency identification results of Section III. In the case studies of this paper, the notch bandwidths are set to fixed values: $\Delta\omega_i = 2\pi \times 9$ kHz$/F_s$, for $i = 1, 2, \ldots, M$, due to the maximum bandwidth of 10 kHz specified by the National Radio Systems Committee (NRSC) for analog AM transmission [25].

B. Optimization Design of Multiple Notch Filter

Particle swarm optimization (PSO) is a computational approach inspired, in part, by bird migration behavior. When PSO is applied to an optimization problem, it iteratively aims to improve a candidate solution (in relation to a success metric) by having a population of candidate solutions (considered particles) that are moved as particle swarms through a

search space according to the mathematical formulas of each particle's position and/or velocity. The fitness of a candidate solution is evaluated at each new position and the iterative particle motion search process continues until a satisfactory solution is achieved [26]–[28].

Algorithm 1 summarizes the basic process of PSO. The effectiveness and convergence of PSO for solving optimization problems has been demonstrated by a large body of literature. To suppress the narrow-band RI characterized in Section III-B, we frame our multiple notch filter design problem as an optimization task [24] such that the magnitude response specifications are satisfied while avoiding a possible ill-conditioning commonly encountered in the all-pass filter design technique [22] and uncontrollable passband gains of classical design approaches [23].

To approximate $H_d(e^{j\omega})$, the system function of an infinite-impulse response multiple notch filter is constructed

$$H(z) = \sum_{i=1}^{M} \frac{1+r_i^2}{2} \frac{(1-e^{j\omega_i}z^{-1})(1-e^{-j\omega_i}z^{-1})}{(1-r_i e^{j\hat{\omega}_i}z^{-1})(1-r_i e^{-j\hat{\omega}_i}z^{-1})} = \sum_{i=1}^{M} \frac{1+r_i^2}{2} \frac{1-2\cos(\omega_i)z^{-1}+z^{-2}}{1-2r_i\cos(\hat{\omega}_i)z^{-1}+r_i^2 z^{-2}} \tag{21}$$

where ω_i is the ith notch frequency, $\hat{\omega}_i$ is the corresponding frequency to be optimized by PSO, and r_i is the polar radius related with notch bandwidth $\Delta\omega_i$

$$r_i = \sqrt{\frac{1-\sin(\Delta\omega_i)}{\cos(\Delta\omega_i)}} \quad \text{or} \quad \Delta\omega_i = \arcsin\left(\frac{1-r_i^4}{1+r_i^4}\right) \tag{22}$$

where $i = 1, 2, \ldots, M$. For system stability, all poles $r_i e^{\pm j\hat{\omega}_i}$ must be placed inside the unit circle in z-plane, i.e., $0 < r_i < 1$. Given the AM bandwidth of $\Delta f_i = 9000$ Hz for the case studies in this paper, we set each notch filter bandwidth to $\Delta\omega_i = \Delta f_i \times 2\pi/F_s$, for $i = 1, 2, \ldots, M$.

For $z = e^{j\omega}$ in (21), the frequency response is given by

$$H(e^{j\omega}) = \sum_{i=1}^{M} \frac{1+r_i^2}{2} \frac{1-2\cos(\omega_i)e^{-j\omega}+e^{-j2\omega}}{1-2r_i\cos(\hat{\omega}_i)e^{-j\omega}+r_i^2 e^{-j2\omega}}. \tag{23}$$

The optimization range for $\hat{\omega}_i$ is set to

$$\left[\hat{\omega}_i^{\min}, \hat{\omega}_i^{\max}\right] = \begin{cases} \left[\dfrac{\omega_1}{2}, \dfrac{\omega_1+\omega_2}{2}\right], & i = 1 \\ \left[\dfrac{\omega_{i-1}+\omega_i}{2}, \dfrac{\omega_i+\omega_{i+1}}{2}\right], & i = 2, \ldots, M-1 \\ \left[\dfrac{\omega_{M-1}+\omega_M}{2}, \dfrac{\omega_M+\pi}{2}\right], & i = M \end{cases} \tag{24}$$

where $\hat{\omega}_i^{\min}$ and $\hat{\omega}_i^{\max}$ are the lower and upper limits, respectively.

To compute $\hat{\omega}_i$ $(i = 1, 2, \ldots, M)$, we apply the full-band minimal error criteria to evaluate the fitness of each particle. Equivalently, PSO filter design aims to minimize the following error between the realized and desired filter frequency responses

$$\min\left\{\int_0^{\pi} \mid H(e^{j\omega}) - H_d(e^{j\omega}) \mid^2 d\omega\right\}. \tag{25}$$

Combining the above optimization idea and the PSO listed in Algorithm 1, we propose a novel multiple notch filter design approach summarized as follows.

Step 1: Obtain the multiple notch filter design specifications: the notch frequency ω_i and corresponding bandwidth $\Delta\omega_i$, for $i = 1, 2, \ldots, M$. The polar radius r_i is computed from $\Delta\omega_i$ using (22).

Step 2: Initialize the particle number K, maximum iteration number $T_{\max}$ and the best fitness value $f_{\text{best}} = g_{\text{best}} = \infty$. Randomly initialize the position $X(t)$ and speed $V(t)$ for each particle whose variables $\hat{\omega}_1, \hat{\omega}_2, \ldots, \hat{\omega}_M$ are to be optimized.

Step 3: For a given iteration t, assign the values of ω_i, r_i and $\hat{\omega}_i$ $(i = 1, 2, \ldots, M)$ in (23) and compute the frequency response of each particle. Then evaluate their fitness, the magnitude response error in the full band $(0 \le \omega \le \pi)$

$$f_{\text{curr}} = \int_0^{\pi} \mid H(e^{j\omega}) - H_d(e^{j\omega}) \mid^2 d\omega. \tag{26}$$

Step 4: For each particle, compare the current fitness f_{curr} with the best fitness f_{best} of itself. If the former is better than the latter, then update the fitness and position of P_{best} with those of P_{curr}.

Step 5: For each particle, compare the current fitness f_{curr} with the best fitness G_{best} of the whole swarm. If the former is better than the later, then the fitness and position of G_{best} are updated by those of P_{curr}.

Step 6: Update the speed and velocity of the kth $(k = 1, 2, \ldots, K)$ particle via the following based on Clerc's constriction method [28], [29] [the reader should note the deviation from (20) used in Algorithm 1]:

$$\begin{cases} V_k(t+1) = wV_k(t) + c_1 s_1(P_k - X_k(t)) \\ \qquad\qquad + c_2 s_2(P_g - X_k(t)) \\ X_k(t+1) = X_k(t) + V_k(t+1) \end{cases} \tag{27}$$

where $w = 0.7289$ and $c_1 = c_2 = 1.4962$; s_1 and s_2 are the random numbers in $[0, 1]$; $-V_{\max} < V_k(t) < V_{\max}$, $V_{\max}$ is the maximum speed; P_k is the best position of the kth particle; and P_g is the best position of all particles.

Step 7: When $t = T_{\max}$ or the design error is less than a predefined precision, terminate and output the optimized results $\hat{\omega}_1, \hat{\omega}_2, \ldots, \hat{\omega}_M$. Otherwise, increment t by 1, go to *Step 3* and begin another iteration.

Step 8: Substitute ω_i, r_i, and $\hat{\omega}_i$ $(i = 1, 2, \ldots, M)$ into (21) or (23) to obtain the system function $H(z)$ or frequency response $H(e^{j\omega})$ of the multiple notch filter.

Once the designed multiple notch filter is applied to the noisy corona current, M narrow-band RI components contained in $x(t)$ are suppressed. This predominantly leaves the residual noise component $n(t)$ that we address using wavelet denoising techniques discussed in Section V.

V. Full-Band Residual Noise Suppression

The wideband nature of $n(t)$ precludes the application of frequency selective filters for its noise removal. Thus, we consider the use of wavelet denoising to remove $n(t)$ from $x(t)$. One reason is that we have assumed that the noise in corona current is additive in Section II-B and there exist a number

of effective filtering methods for additive noise in the wavelet domain. Second, wavelet denoising can be adaptively applied by implementing variable thresholding of wavelet coefficients based on localized signal regularity [30]. This makes it a suitable choice when there is a lack of prior knowledge of the characteristics of HVdc corona current.

The continuous wavelet transform of $f(t) \in L^2$ is defined as

$$F(a,b) = \frac{1}{\sqrt{a}} \int_{-\infty}^{\infty} f(t)\psi^* \left(\frac{t-b}{a}\right) dt \tag{28}$$

where $a > 0$ and $-\infty < b < \infty$; a and b are the scale and translation parameters related with frequency and location, and $\psi(t)$ is the wavelet function (mother wavelet). Equation (28) can be discretized on a time-frequency grid by employing $a = 2^j$ and $b = k \cdot 2^j$, for $j, k \in \mathbb{Z}$ to give the following discrete wavelet transform (DWT):

$$F(j,k) = \frac{1}{\sqrt{2^j}} \int_{-\infty}^{\infty} f(t)\psi^* \left(\frac{t-2^j k}{2^j}\right) dt. \tag{29}$$

In the resulting *multiresolution pyramid* for wavelet expansion, $f(t)$ can be mathematically expressed by [30]–[32]

$$f(t) = \sum_{k=-\infty}^{\infty} c_{j_0,k}\phi_{j_0,k}(t) + \sum_{j=0}^{\infty}\sum_{k=-\infty}^{\infty} d_{j,k}\psi_{j,k}(t) \tag{30}$$

where the first term represents the approximation information at an arbitrary starting scale j_0 and the second term represents the sum of detailed information of the original signal $f(t)$. The approximation coefficients $c_{j_0,k}$ and the detail coefficients $d_{j,k}$ are calculated by

$$\begin{cases} c_{j_0,k} = \displaystyle\int_{-\infty}^{\infty} f(t)\phi^*_{j_0,k}(t)dt \\ d_{j,k} = \displaystyle\int_{-\infty}^{\infty} f(t)\psi^*_{j,k}(t)dt \end{cases} \tag{31}$$

where $\phi_{j_0,k}(t)$ and $\psi_{j,k}(t)$ are, respectively, obtained from the scale function $\phi(t)$ and the mother-wavelet $\psi(t)$

$$\begin{cases} \phi_{j_0,k}(t) = \dfrac{1}{\sqrt{2^{j_0}}}\phi\left(\dfrac{t-2^{j_0}k}{2^{j_0}}\right) \\ \psi_{j,k}(t) = \dfrac{1}{\sqrt{2^j}}\psi\left(\dfrac{t-2^j k}{2^j}\right). \end{cases} \tag{32}$$

The multiresolution analysis simplifies the calculation of the coefficients $c_{j_0,k}$ and $d_{j,k}$. It can be implemented using two-channel filter banks with Mallat's algorithm [30] to enhance computational efficiency. The coefficient calculation method and fractionated spectrum (producing *sub-bands*) of a three-level wavelet decomposition are shown in Fig. 7.

In the discrete wavelet decomposition of the notch filtered corona current $x(t)$, the wideband noise $n(t)$ is considered to be disseminated to all sub-bands. In contrast to the standard frequency domain, the corona current is considered to have greater coefficient compaction properties thus providing greater separation between the signal of interest and noise. Thus, wavelet coefficients that are considered to include wideband noise components alone (specified through a given property) may be attenuated to zero while preserving

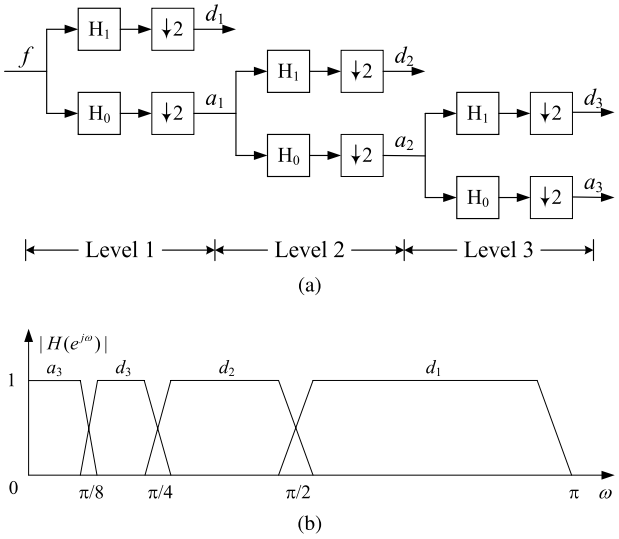

Fig. 7. Three-level wavelet decomposition and its fractionated spectrum. (a) Wavelet decomposition. (b) Fractionated spectrum.

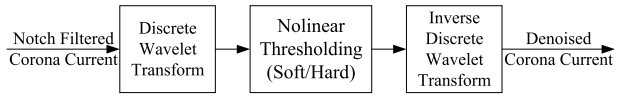

Fig. 8. DWT-based denoising schematic for residual noise removal.

the coefficients containing the corona current. The resulting inverse DWT produces a noise-reduced corona signal.

The proposed full-band noise reduction schematic is shown in Fig. 8. The selection of wavelet function (including scale function $\phi(t)$ and wavelet function $\psi(t)$) has great impact on full-band noise suppression. Daubechies wavelets are selected because they are orthogonal and exhibit maximal vanishing moments for given supports. They can reduce Gibbs phenomena and produce larger coefficients, which we assert will help to separate the residual noise from corona current.

The thresholding strategy also plays an important role in noise reduction. If a wavelet coefficient is lower than a specific threshold, it is considered noise and treated afterward. A large threshold may result in oversmoothing, while a smaller one may permit excessive noise. There are two kinds of thresholding methods—hard

$$Z' = \begin{cases} Z, & \text{if } |Z| > \delta \\ 0, & \text{otherwise} \end{cases} \tag{33}$$

and soft

$$Z' = \begin{cases} Z - \delta, & Z \geq \delta \\ Z + \delta, & Z \leq -\delta \\ 0, & |Z| < \delta \end{cases} \tag{34}$$

where Z is a wavelet coefficient and δ is a threshold [30], [34]. Fig. 9 demonstrates that the hard thresholding *keeps* the coefficient above the threshold while soft thresholding *shrinks* the coefficient above the threshold.

There are four well-known ways to assign the threshold value δ: 1) *rigrsure*: based on Stein's unbiased estimation of risk; here, risk is minimized for a threshold value;

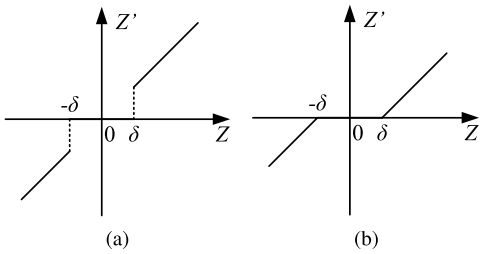

Fig. 9. Hard and soft thresholding for wavelet denoising. (a) Hard thresholding. (b) Soft thresholding.

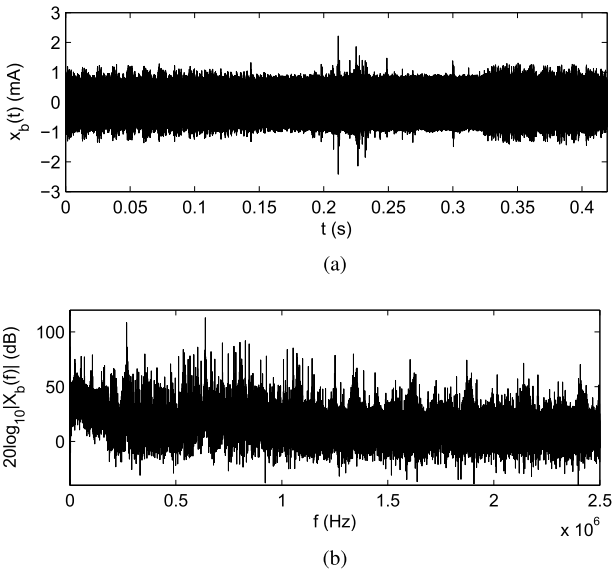

Fig. 10. Waveform and spectrum of measured background noise (0 kV) of HVdc transmission lines. (a) Waveform. (b) Spectrum (dB).

2) *sqtwolog*: that uses a fixed-form threshold that yields mini–max performance multiplied by a small factor; 3) *heursure*: representing a mixture of the two previous options, but the fixed threshold is used for small signal-to-noise ratio (SNR); and 4) *minimaxi*: that uses a fixed threshold to realize the minimum of the maximum mean square error obtained for the worst function. The denoised results from different thresholds are compared in Section VI. The reader should note that the adaptive thresholds can also be used to obtain better values. After wavelet-based denoising, the results are applied to estimate the CL of HVdc transmission lines, which is beyond the scope of this paper.

VI. Experimental Results and Analysis

To evaluate the performance of the proposed noise suppression method, we obtain the measurements of background noise and corona current corresponding to 0 and −800 kV, respectively, on the transmission lines. The measurements are recorded by the measurement system (discussed in Section II-A) at the HVdc Experimental Base of the China Electric Power Research Institute. The measured background noise and corona current are shown in Figs. 10 and 11, respectively. In order to show spectra on a reasonable scale

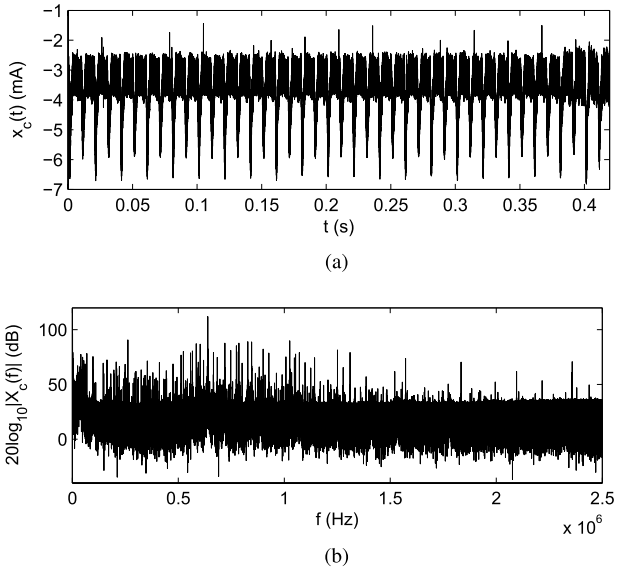

Fig. 11. Waveform and spectrum of measured noisy corona current (−800 kV) of HVdc transmission lines. (a) Waveform. (b) Spectrum (dB).

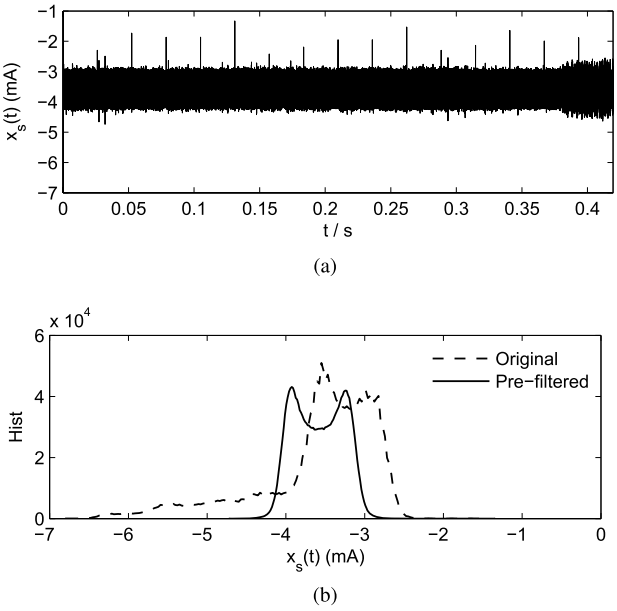

Fig. 12. Waveform and histogram of prefiltered corona current. (a) Waveform. (b) Histogram.

of detail, the dc components have been removed, which has also been Fig. 13 and Fig. 15.

In Fig. 11, the low-frequency harmonics ($\leq$ 2000 Hz) from rectification effects (nonideal converter from HVAC to HVdc) can be observed and must be removed in advance of the proposed filtering approach. The waveform and histogram of the prefiltered corona current are shown in Fig. 12. Although the waveform quality has been enhanced (SNR improves 7.70 dB by prefiltering), the CL is still difficult to estimate given the non-Gaussian nature of the asymmetric and bimodal distribution which makes typical noise-reduction techniques inapplicable.

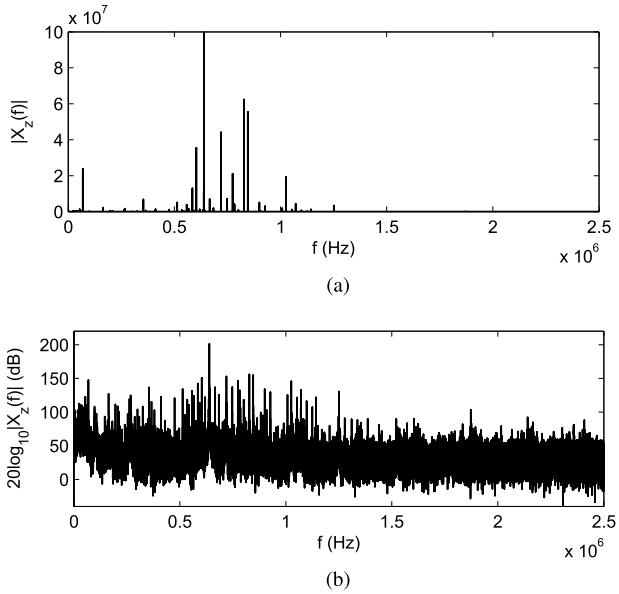

Fig. 13. Cross correlation function spectrum of prefiltered corona current and background noise. (a) Spectrum. (b) Spectrum (dB).

TABLE II
EIGHT STRONGEST COMPONENTS SELECTED FROM FIG. 13
($\omega_i = 2\pi f_i/F_s, i = 1, 2, \ldots, 8$, WHERE $F_s = 5 \times 10^6$ Hz)

i	f_i (kHz)	ω_i/π	i	f_i (kHz)	ω_i/π
1	68.5	0.0274	**5**	783	0.3132
2	603	0.2412	**6**	828	0.3312
3	639	0.2556	**7**	846	0.3384
4	720	0.2880	**8**	1071	0.4284

Comparing Figs. 10 and 11, we observe that there are significant peaks located at selecting frequencies. Upon further inspection, they are primarily from the carrier components of AM radio broadcasts. To recognize them accurately, the cross correlation function of the background noise and prefiltered corona current is calculated in the frequency domain and shown in Fig. 13.

From Fig. 13, we observe that some spectral lines are significantly enhanced by the cross correlation function operation. The eight most significant frequencies are selected and listed in Table II. Except for the component at 68.5 kHz representing a long-wave timing signal, all frequencies are the result of AM broadcasts. For example, the strongest peak at 639 kHz represents the carrier frequency of the Voice of China in Beijing, China.

To remove the narrow-band components of the prefiltered corona current whose center frequencies are recognized by the cross correlation function operation and listed in Table II, a multiple notch filter is optimally designed by the PSO-based method discussed in Section IV whereby as discussed all notch bandwidths are set to 9 kHz (slightly narrower than the maximum bandwidth of 10 kHz specified by NRSC [25] for analog AM transmission, in our case study).

The magnitude response of the designed multiple notch filter is shown in Fig. 14 and achieves better performance over the cascading design method [23]. The waveform and spectrum

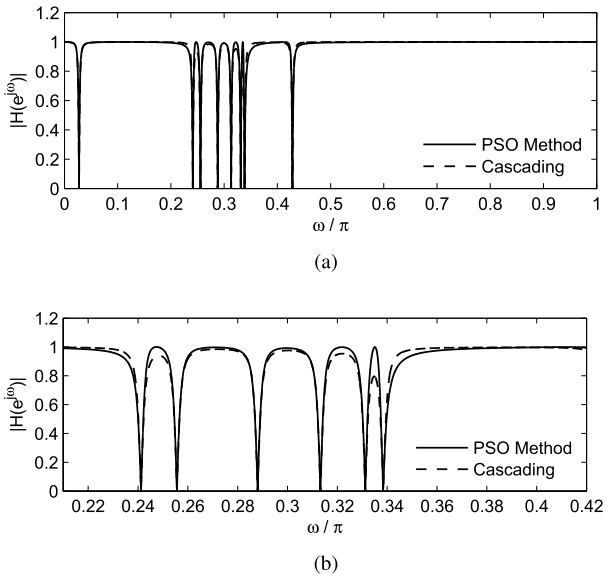

Fig. 14. Magnitude response of multiple notch filter designed by PSO. (a) Overall magnitude response: $\omega \in [0, \pi]$. (b) Expanded magnitude response: $\omega \in [0.21\pi, 0.42\pi]$.

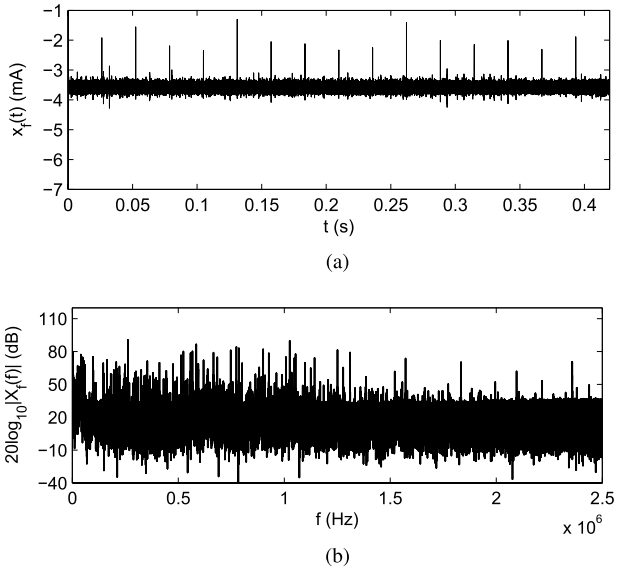

Fig. 15. Waveform and spectrum of notch filtered corona current. (a) Waveform. (b) Spectrum (dB).

of the notch filtered corona current are shown in Fig. 15. As evident, the eight narrow-band components in Table II are effectively eliminated to enhance the corona current waveform quality (SNR improves 12.51 dB by notch filtering). However, it is also clear that the residual full-band noise remains requiring the use of wavelet denoising techniques.

We provide the denoising results for three instances of our approach at decomposition levels $L = 2, 5, 8$ using Daubechies wavelets db-4 and hard thresholding with the mini–maxi method in Fig. 16. In order to study the impacts of Daubechies wavelets (db-N, $N = 1, 2, \ldots, 45$) and decomposition levels, the denoising performance (characterized by SNR) of the proposed approach are evaluated under different conditions, as shown in Fig. 17. When $L < 12$, SNR is

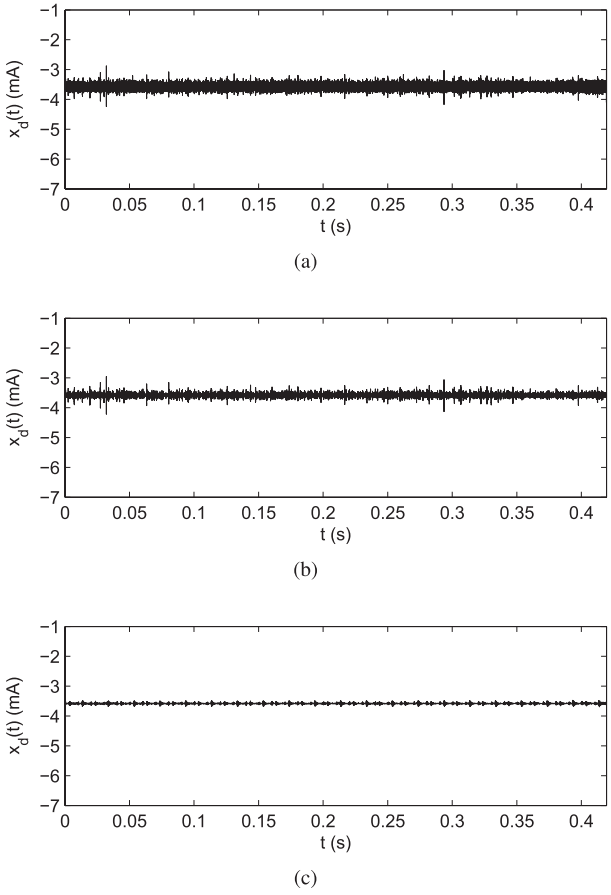

Fig. 16. Denoised waveforms related with different wavelet decomposition levels (characterized by L). (a) $L = 2$. (b) $L = 5$. (c) $L = 8$.

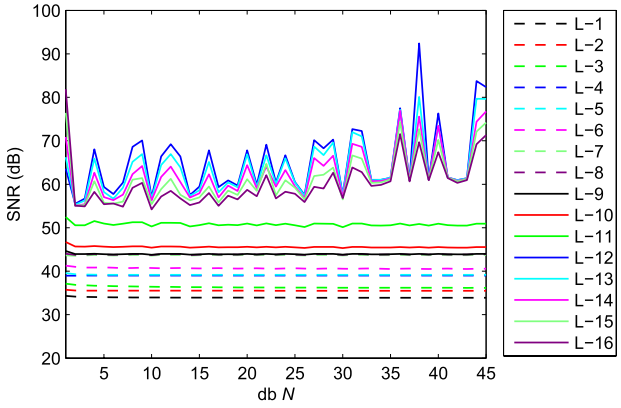

Fig. 17. Denoising performance (SNR) impacted by Daubechies wavelet functions (characterized by N) and decomposition levels.

almost unaffected by the value of N and *increases* as L increases. When $L \geq 12$, SNR is affected by the value of N and *decreases* as L increases, which is the result of excessive decomposition of the corona current. From our tests, we observe that $L = 12$ is an optimal decomposition level to obtain high SNR at almost all values of N.

We observe that when $L = 12$ and $N = 9$ (db-9) in Fig. 17, there is a high value for SNR. One should note that for the same decomposition level, other wavelet functions, for example db-38, obtain higher SNR, but the computational complexity is significantly higher for increasing

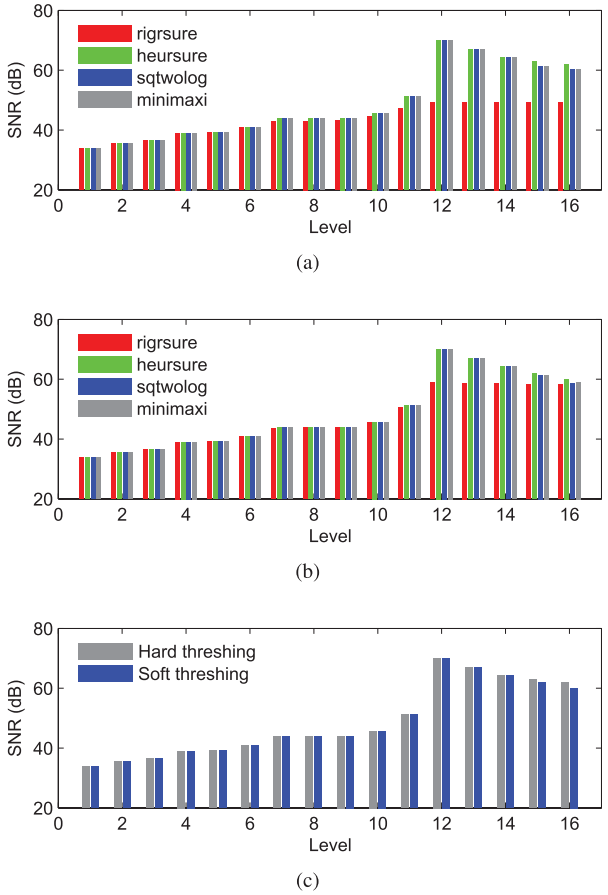

Fig. 18. Denoising performance impacted by wavelet decomposition levels and thresholding methods (wavelet function db-9). (a) Hard thresholding. (b) Soft thresholding. (c) Hard versus soft thresholdings (heursure).

the values of N. In practice, we recognize that an SNR of 60 dB produces a good degree of noise suppression of corona current. Hence, we assert that db-9 is a right choice to achieve an appropriate tradeoff between denoising performance and computational efficiency in our case study.

We next apply the db-9 wavelet to analyze the impacts of the hard and soft thresholdings on denoising performance. Fig. 18 shows that the rigrsure method applied to assign a δ value in Fig. 9 produces larger error than the other three methods. It also shows that there is a negligible difference (for $N \leq 14$) between the hard and soft thresholdings, which is not true in the case of other wavelet functions and decomposition levels. Adaptive thresholds [33] can be used to enhance the denoising performance, but is beyond the scope of this paper. Figs. 17 and 18 demonstrate that selection of the decomposition levels is extremely important for our noise suppression approach.

Using the Daubechies wavelet db-9, a decomposition level of $L = 12$, and hard thresholding via the heursure method, the denoised corona current is shown in Fig. 19. We observe that the interference components are suppressed sufficiently (SNR improves 36.39 dB with wavelet denoising) and the denoised waveform looks like a horizontal line. This is consistent with the assumption provided in Section III-A that states the noiseless corona current is a constant value in statistical sense.

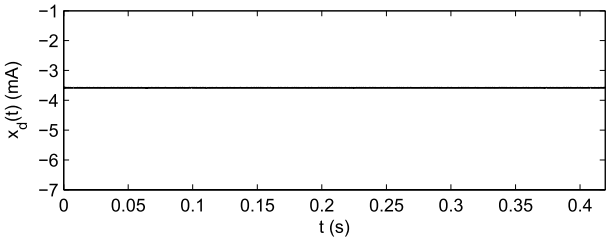

Fig. 19. Denoised waveform of corona current (wavelet function db-9, heursure method, and decompostion level $L = 12$).

Fig. 19 provides a convenient way to calculate the corona current value and then estimate the CL of HVdc transmission lines, of which the latter part is beyond the scope of this paper.

From the above experiments involving our proposed noise suppression approach shown in Fig. 5, we conclude the following.

1) The cross correlation function method significantly reduces the difficulties in recognizing the narrow-band RI components.
2) The PSO-based multiple notch filter design method obtains better magnitude response to remove the narrow-band interference components.
3) The wavelet-based denoising techniques sufficiently reduce the residue full-band noise using db-9 wavelet, decomposition level $L = 12$, and hard thresholding heursure method in our case study.

VII. Conclusion

This paper proposes a novel noise suppression method applicable to the measured corona current on HVdc transmission lines. Our approach considers the narrow-band RI components separately from wideband components thus resulting in the stages of filtering that are adapted to the characteristics of the noise they suppress. Thus, a main contribution of this paper is a multistage noise suppression framework for HVdc corona current measurements, which sequentially integrates narrow-band RI removal and wideband residual noise reduction. First, we propose a cross correlation function-based approach to recognize the center frequencies of narrow-band RI components. It provides the design frequencies for a multiple notch filter employed for narrow-band RI suppression. Next, we make use of PSO for the design of the multiple notch filter that demonstrates superior magnitude response characteristics to the well-known cascading method. Then, we employ wavelet denoising techniques with hard and soft thresholds to reduce the residual wideband noise. Finally, the performance of the proposed noise suppression method is validated using onsite measured corona current signals. Thus, the method can be easily realized to support the analysis and estimation of CL of HVdc transmission lines.

Future work associated with this paper will focus on the development of time-varying mathematical models of the measured corona current and background noise taking into account nonlinear nonstationary characteristics and the presence of leakage current in the sensing process, the design of a linear-phase multiple notch filter, and the estimation of CL and secondary effects of HVdc transmission lines.

References

[1] C. Fang, X. Cui, X. Zhou, T. Lu, Y. Zhen, and X. Li, "Impact factors in measurements of ion-current density produced by high-voltage DC wire's corona," *IEEE Trans. Power Del.*, vol. 28, no. 3, pp. 1414–1422, Jul. 2013.

[2] H. Yuan, Q. Yang, Y. Liu, J. Lu, and S. A. Akhtar, "Development and application of high-frequency sensor for corona current measurement under ultra high-voltage direct-current environment," *IEEE Trans. Instrum. Meas.*, vol. 61, no. 4, pp. 1064–1071, Apr. 2012.

[3] M. P. Sarma and W. Janischewskyj, "Analysis of corona losses on DC transmission lines: I—Unipolar lines," *IEEE Trans. Power App. Syst.*, vol. PAS-88, no. 5, pp. 718–731, May 1969.

[4] R. G. Urban, H. C. Reader, and J. P. Holtzhausen, "Small corona cage for wideband HVac radio noise studies: Rationale and critical design," *IEEE Trans. Power Del.*, vol. 23, no. 2, pp. 1150–1157, Apr. 2008.

[5] A. Hebra, "The reality of generation and distribution of electric power, part 2: The other face of ultrahigh voltage power transmission," *IEEE Instrum. Meas. Mag.*, vol. 15, no. 3, pp. 22–30, Jun. 2012.

[6] P. S. Maruvada, "Influence of ambient electric field on the corona performance of HVdc transmission lines," *IEEE Trans. Power Del.*, vol. 29, no. 2, pp. 691–698, Apr. 2014.

[7] P. S. Maruvada, "Electric field and ion current environment of HVdc transmission lines: Comparison of calculations and measurements," *IEEE Trans. Power Del.*, vol. 27, no. 1, pp. 401–410, Jan. 2012.

[8] P. S. Maruvada, *Corona Performance of High-Voltage Transmission Lines*. Baldock, U.K.: Taylor & Francis Group, 2000.

[9] Z. M. Al-Hamouz, "Corona power loss, electric field, and current density profiles in bundled horizontal and vertical bipolar conductors," *IEEE Trans. Ind. Appl.*, vol. 38, no. 5, pp. 1182–1189, Sep./Oct. 2002.

[10] Z. M. Al-Hamouz, M. Abdel-Salam, and A. Mufti, "Improved calculation of finite-element analysis of bipolar corona including ion diffusion," *IEEE Trans. Ind. Appl.*, vol. 34, no. 2, pp. 301–309, Mar./Apr. 1998.

[11] A. J. Otto and H. C. Reader, "HVDC corona space charge modeling and measurement," *IEEE Trans. Power Del.*, vol. 26, no. 4, pp. 2630–2637, Oct. 2011.

[12] P. Wang and G. Zhang, "The measurement method for corona discharge current under high-voltage environment," *IEEE Trans. Instrum. Meas.*, vol. 57, no. 8, pp. 1786–1790, Aug. 2008.

[13] M. Xu, Z. Tan, and K. Li, "Modified peek formula for calculating positive DC corona inception electric field under variable humidity," *IEEE Trans. Dielectr. Electr. Insul.*, vol. 19, no. 4, pp. 1377–1382, Aug. 2012.

[14] V. L. Chartier, D. F. Shankie, and N. Kolcio, "The Apple Grove 750-kV project: Statistical analysis of radio influence and corona-loss performance of conductors at 775 kV," *IEEE Trans. Power App. Syst.*, vol. PAS-89, no. 5, pp. 867–881, May 1970.

[15] X. Bian, L. Wang, J. M. K. MacAlpine, Z. Guan, J. Hui, and Y. Chen, "Positive corona inception voltages and corona currents for air at various pressures and humidities," *IEEE Trans. Dielectr. Electr. Insul.*, vol. 17, no. 1, pp. 63–70, Feb. 2010.

[16] S. Sriram, S. Nitin, K. M. M. Prabhu, and M. J. Bastiaans, "Signal denoising techniques for partial discharge measurements," *IEEE Trans. Dielectr. Electr. Insul.*, vol. 12, no. 6, pp. 1182–1191, Dec. 2005.

[17] D. Evagorou, A. Kyprianou, P. L. Lewin, A. Stavrou, V. Efthymiou, and G. E. Georghiou, "Evaluation of partial discharge denoising using the wavelet packets transform as a preprocessing step for classification," in *Proc. Annu. Rep. Conf. Elect. Insul. Dielectr. Phenomena*, Oct. 2008, pp. 387–390.

[18] S. V. Vaseghi, *Advanced Digital Signal Processing and Noise Reduction*. West Sussex, U.K.: Wiley, 2008.

[19] A. J. Otto and H. C. Reader, "Wideband and narrowband HVDC conductor corona test methods for radio noise prediction," *IEEE Trans. Power Del.*, vol. 25, no. 4, pp. 2950–2957, Oct. 2010.

[20] B. Girod, *Signals and Systems*. West Sussex, U.K.: Wiley, 2001.

[21] D. G. Manolakis, V. K. Ingle, and S. M. Kogon, *Statistical and Adaptive Signal Processing: Spectral Estimation, Signal Modeling, Adaptive Filtering and Array Processing*. Norwood, MA, USA: Artech House, 2005.

[22] S.-C. Pei and C.-C. Tseng, "IIR multiple notch filter design based on allpass filter," *IEEE Trans. Circuits Syst. II, Analog Digit. Signal Process.*, vol. 44, no. 2, pp. 133–136, Feb. 1997.

[23] S. Yimman, S. Praesomboon, P. Soonthuk, and K. Dejhan, "IIR multiple notch filters design with optimum pole position," in *Proc. Int. Symp. Commun. Inf. Technol. (ISCIT)*, Oct./Sep. 2006, pp. 281–286.

[24] C.-C. Tseng and S.-C. Pei, "Stable IIR notch filter design with optimal pole placement," *IEEE Trans. Signal Process.*, vol. 49, no. 11, pp. 2673–2681, Nov. 2001.
[25] National Radio Systems Committee, *NRSC AM Preemphasis/Deemphasis and Broadcast Audio Transmission Bandwidth Specifications*, NRSC Standard NRSC-1-B, Arlington, VA, USA, 2012.
[26] J. Kennedy and R. Eberhart, "Particle swarm optimization," in *Proc. IEEE Int. Conf. Neural Netw.*, vol. 4. Nov./Dec. 1995, pp. 1942–1948.
[27] D. Bratton and J. Kennedy, "Defining a standard for particle swarm optimization," in *Proc. IEEE Swarm Intell. Symp. (SIS)*, Apr. 2007, pp. 120–127.
[28] M. Clerc and J. Kennedy, "The particle swarm—Explosion, stability, and convergence in a multidimensional complex space," *IEEE Trans. Evol. Comput.*, vol. 6, no. 1, pp. 58–73, Feb. 2002.
[29] R. Poli, J. Kennedy, and T. Blackwell, "Particle swarm optimization: An overview," *Swarm Intell.*, vol. 1, no. 1, pp. 33–57, 2007.
[30] S. Mallat, *A Wavelet Tour of Signal Processing: The Sparse Way*, 3rd ed. Burlington, MA, USA: Academic, 2009.
[31] E. C. T. Macedo *et al.*, "Wavelet transform processing applied to partial discharge evaluation," *J. Phys., Conf. Ser.*, vol. 364, no. 1, p. 012054, 2012.
[32] D. Labate, F. L. Foresta, G. Occhiuto, F. C. Morabito, A. Lay-Ekuakille, and P. Vergallo, "Empirical mode decomposition vs. wavelet decomposition for the extraction of respiratory signal from single-channel ECG: A comparison," *IEEE Sensors J.*, vol. 13, no. 7, pp. 2666–2674, Jul. 2013.
[33] X. Ma, C. Zhou, and I. J. Kemp, "Automated wavelet selection and thresholding for PD detection," *IEEE Elect. Insul. Mag.*, vol. 18, no. 2, pp. 37–45, Mar./Apr. 2002.
[34] D. L. Donoho, "De-noising by soft-thresholding," *IEEE Trans. Inf. Theory*, vol. 41, no. 3, pp. 613–627, May 1995.

Qiusheng Wang received the B.A.Sc., M.A.Sc., and Ph.D. degrees from the Harbin Institute of Technology, Harbin, China, in 1996, 1998, and 2002, respectively.

He was a Post-Doctoral Fellow with the Institute of Computing Technology, Chinese Academy of Sciences, Beijing, China, in 2004. From 2013 to 2014, he was a Visiting Scholar with the Department of Electrical and Computer Engineering, University of Toronto, Toronto, ON, Canada. Since 2004, he has been an Associate Professor with the School of Automation Science and Electrical Engineering, Beihang University, Beijing. His current research interests include digital signal processing, cyber-security of smart grid, cyber-physical system theory, computation intelligence, digital image processing, and integrated system health management.

Deepa Kundur (F'15) received the B.A.Sc., M.A.Sc., and Ph.D. degrees from the University of Toronto, Toronto, ON, Canada, in 1993, 1995, and 1999, respectively, all in electrical and computer engineering.

She was an Assistant Professor with the Edward S. Rogers Sr. Department of Electrical and Computer Engineering, University of Toronto, from 1999 to 2002, and returned to hold the title of Professor in 2012. From 2003 to 2012, she was a Faculty Member in Electrical and Computer Engineering with Texas A&M University, College Station, TX, USA. Her current research interests include modeling, analysis and signal processing for smart grid, cyber-physical system theory, and multimedia security and forensics.

Dr. Kundur has been on several editorial boards and currently serves as an Associate Editor of the IEEE TRANSACTIONS ON INFORMATION FORENSICS AND SECURITY. She has served on the North American Reliability Corporation Smart Grid Task Force. Her research has received best paper recognitions at the 2008 IEEE INFOCOM Workshop on Mission Critical Networks, the 2011 Cyber Security and Information Intelligence Research Workshop, and the 2012 IEEE Canadian Conference on Electrical and Computer Engineering.

Haiwen Yuan received the B.Sc., M.Sc., and Ph.D. degrees in electrical engineering from Xi'an Jiaotong University, Xi'an, China, in 1990, 1993, and 1996, respectively.

He has been a Professor with the School of Automation Science and Electrical Engineering, Beihang University, Beijing, China, since 2003. His current research interests include special power supply and advanced measurement technology.

Yuanqing Liu was born in Henan, China, in 1980. He received the B.S. degree in electrical engineering from Chongqing University, Chongqing, China, in 2003, and the Ph.D. degree from Tsinghua University, Beijing, China, in 2009.

He became an Engineer with the China Electric Power Research Institute, Beijing, in 2009. His current research interests include electromagnetic environment of ultrahigh-voltage dc transmission line.

Jiayu Lu was born in Hubei, China, in 1957. He received the B.S. degree from Shanghai Jiaotong University, Shanghai, China, in 1981, the master's degree from the Huazhong University of Science and Technology, Wuhan, China, and the Ph.D. degree from Xi'an Jiaotong University, Xi'an, China, in 1996.

His current research interests include power systems electromagnetic environment and compatibility.

Zhao Ma was born in Shaanxi, China, in 1957. He received the B.S. degree from Xi'an Jiaotong University, Xi'an, China, in 1982, and the Ph.D. degree from Staffordshire University, Staffordshire, U.K., in 1996.

His current research interests include electric power engineering, power transmission, and distribution technologies.